Covalent coupling of DNA bases with graphene nanoribbon electrodes: Negative differential resistance, rectifying, and thermoelectric performance*

Peng-Peng Zhang(张鹏鹏)[1], Shi-Hua Tan(谭仕华)[1,†], Xiao-Fang Peng(彭小芳)[1,‡], and Meng-Qiu Long(龙孟秋)[2]

[1] *Hunan Provincial Key Laboratory of Materials Surface or Interface Science and Technology, Central South University of Forestry and Technology, Changsha* 410004, *China*

[2] *School of Physics and Electronics, Central South University, Changsha* 410083, *China*

(Received 16 June 2020; revised manuscript received 18 July 2020; accepted manuscript online 28 July 2020)

By applying nonequilibrium Green's functions in combination with the density-functional theory, we investigate the electronic, thermal, and thermoelectric properties of four kinds of bases in DNA perpendicularly coupling between two ZGNR electrodes. The results show that the electron transport is highly sensitive to different base-ZGNR coupling geometries, and the system can present large rectifying and negative differential resistance effects. Moreover, the fluctuations of electronic transmission and super-low thermal conductance result in significant enhancement of the thermoelectric figure of merit (ZT): the ZT will be over 1.4 at room temperature, and over 1.6 at 200 K. The results show that the base-ZGNR coupling devices can present large rectifying, negative differential resistance, and enhanced thermoelectric effects.

Keywords: DNA bases, graphene, electron transport, phonon transport, thermoelectric performance

PACS: 68.65.–k, 44.10.+i, 65.80.Ck, 81.05.Ue **DOI:** 10.1088/1674-1056/aba9bf

1. Introduction

Single-molecule devices have garnered much attention in recent years for their potential applications in the next generation of electronic devices.[1–15] Many novel functional single-molecule devices have been designed, and a number of fascinating charge transport properties are found such as negative differential resistance (NDR), rectifying effect (RE), and thermoelectric energy conversion.[16–23] NDR effect is characterized by a negative slope in the I–V curve, which can be used in a wide range of applications such as frequency multipliers, fast switches, memory, high-frequency oscillators.[23] Furthermore, heat and electricity are two different forms of energy, and thermoelectric devices (TE) can offer direct thermal-to-electrical energy conversion, including waste heat and solar energy to electricity. The efficiency of thermoelectrics can be measured using the thermoelectric figure of merit. The single molecules with multi-functional properties will occupy an important position in the future. In particular, due to graphene extraordinary mechanical, physical,[24–26] and chemical properties,[27] graphene-based single-molecule devices have attracted extensive interest in recent years. Based on the existing planar carve technologies, graphene can be patterned into quasi-one-dimensional material, graphene nanoribbon (GNR), which can be classified as zigzag (ZGNR for zigzag GNR) and armchair depending on their edge geometry. The edge styles and widths were found to play a pivotal role in the charge-transport properties. Until now, many interesting physical effects have been revealed in these quantum structures by coupling GNRs with moleculars.[28] For instance, the studies reported that the functionalized-GNR hybrid structure with porphyrins only can not improve the solubility and dispersion stability[24] but also presents NDR.[29] By the density functional theory, Wu revealed that the $Mn(dmit)_2$ molecule-based molecular device with two ZGNR electrodes can present large RE.[19] Furthermore, good TE[30] also were reported in graphene-based topological insulators with heavy adatoms and nanopores[31] or ZGNR with gold atom chains at the edges.[32] Such studies have aroused keen interest among the multifunctional single-molecule devices by connecting GNRs with various molecules. More interestingly, DNA, a star of molecules, can be accurately high-speed sequencing by GNRs,[33] which is promising to monitor modulations in the currents running through GNR on interaction with DNA bases[19] (note that there are four kinds of bases in DNA: adenine, cytosine, thymine, guanine (in the following abbreviated as A, C, T, G)). A deep understanding of the mechanisms underpinning the operation of the base-GNR coupling devices is therefore very important for the design and production of functionalized base-GNR coupling devices. However, the research in this area is still lacking.

*Project supported by the National Natural Science Foundation of China (Grant Nos. 11704417 and 11247030), the Natural Science Foundation of Hunan Province, China (Grant No. 2019JJ40532), and the Talent Introducing Foundation of Central South University of Forestry and Technology (Grant No. 104-0160).

†Corresponding author. E-mail: shtan@csuft.edu.cn

‡Corresponding author. E-mail: xiaofangpeng11@163.com

Covalent linking of bases to GNRs could open the opportunity to create organic single-molecule devices with extraordinary transport properties. In the present work, we investigate the electron transport properties of GNRs with different bases. On the basis of first-principles calculations, we find very interesting transport properties in these base-molecule devices. More interestingly, large RE and NDR behaviors are also observed. Moreover, the ZT can be improved obviously, and the $ZT_{\max}$ will be over 1.4 at room temperature, and over 1.6 at 200 K. These results are constructive for the practical applications of molecular devices.

2. Method and model

It is known that DNA is a double spiral structure with π–π stacking between neighboring bases. The real direction of charge transfer is vertical to the surface of the DNA bases. Inspired by this structure, the bases are designed to couple perpendicularly with N-ZGNR in this paper.

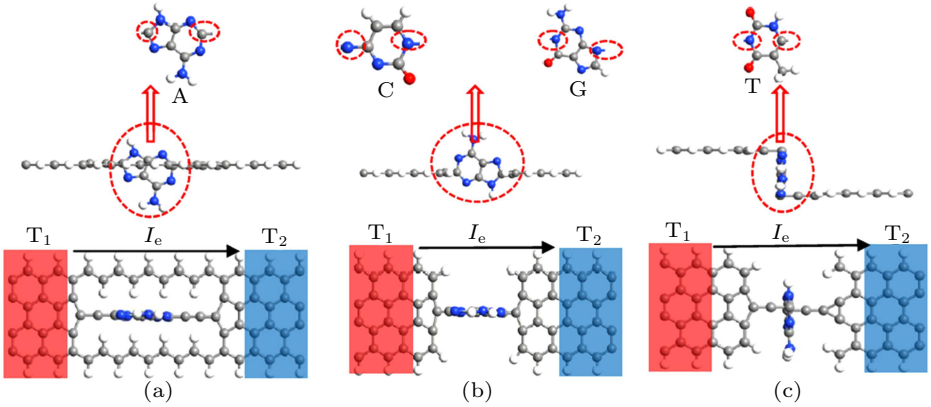

Fig. 1. Schematic diagram of three kinds of base-ZGNR coupling devices (the bases are all sandwiched perpendicularly between two infinite N-ZGNR electrodes): (a) the base is parallel to the zigzag edges and the zigzag edges keep perfect in the structures (N-AGNR-I-(a)), (b) the base is parallel to the zigzag edges and the zigzag edges are disconnected in the scattering region (N-AGNR-I-(b)), (c) the base is vertically to the zigzag edges, and the left and right electrodes are non-coplanar (N-AGNR-I-(c)).

The molecular devices we studied are illustrated in Fig. 1, which display three coupling configurations, namely N-AGNR-I-(a), N-AGNR-I-(b), and N-AGNR-I-(c) (N is the number of carbon dimer lines across the ribbon width, and I represents the types of bases). Here, the bottom-row figures are the top view, the middle-row figures are side view, the top-row figures are the structures of A, C, G, T bases, and the atoms with red circle markers are the atoms bonded with the electrodes. The three coupling configurations are divided into three regions: left and right N-ZGNR electrodes, and central scattering region. The geometrical optimization of the model structures and the transport properties are all performed by using the ATOMISTIXTOOLKIT (ATK) package. ATK is a powerful set of modeling tools for investigating a variety of nanoscale systems such as molecules, bulk and two-probe systems. The systems may contain nanowires, nanotubes, graphene, high-k dielectric interfaces, semiconductors, metals, *etc*., and the calculations are based on the following techniques: density-functional theory (DFT), extended Hückel theory, classical potentials, and non-equilibrium Green's functions (NEGF). The overview of the work flow is: Building Atomistic Structures, Script Generator, Job Manager, Analyzing the Results. The specific calculation see the official website for specific operation methods and steps. (https://docs.quantumwise.com/index.html) For carbon materials, using single-plus polarization basis and 150 Ry (1 Ry = 13.6056923(12) eV) of cutoff energy is enough to ensure the accuracy of calculation.[34,35] Within the frame of NEGF in combination with the DFT, local density approximation (LDA) is preferable at handling electronic transport in device under open boundary conditions.[34,35] In order to examine the accuracy of the obtained results, a comparison of the achieved data to those experimentally supplied in literature was performed. The calculation results using LDA are highly consistent with the experiments.[36–38] ATK calculation manual indicates that for a calculation of a system like electrode–molecule–electrode with a molecule along the Z axis and the transport direction also along the Z direction, since the system has no periodicity in x–y direction, one should therefore not need more than one k-point in this direction. In the Z direction, however, the self-energy calculation effectively corresponds to an infinite number of k-points, and we need a lot of k-points in the electrode calculation to match the electronic structures of the electrodes and the central region. The calculations should be safe to stick to 100 k-points along the C direction. So, in the calculations, the cutoff energy is set to 150 Ry, and $1\times1\times100$ k-point mesh is used. The structure in the device region is relaxed until the forces acting on the atoms dropped below 0.05 eV/Å. Moreover, a large enough vacuum layer ($>$ 15 Å) is applied to keep the device from any interaction with its mirror images both in ATK calculation, and all the dangling bonds of edge carbon atoms are passivated with hydrogen atoms. At finite bias, the current can be expressed as:[39–42]

$$I(V_{\rm b}) = \frac{G_0}{e}\int \tau_{\rm e}(E,V_{\rm b})\,[f_{\rm l}(E-\mu_{\rm l}) - f_{\rm r}(E-\mu_{\rm r})]\,{\rm d}E, \quad (1)$$

where $G_0 = 2e^2/h$ is the conductance quantum, $\mu_l - \mu_r = eV_b$, μ_l, and μ_r are electrochemical potentials of the left (right) electrode. $f_l(E-\mu_l)$ and $f_r(E-\mu_r)$ are the Fermi–Dirac distribution functions, which can be expressed as

$$f_{l(r)}(E-\mu_{l(r)}) = \frac{1}{\exp\left[(E-\mu_{l(r)})/\kappa_B T\right]+1}, \tag{2}$$

$\tau_e(E,V_b)$ is the transmission coefficient for the left electrode across the scattering region into the right electrode, which is the key issue to predict the current and can be expressed as

$$\tau_e(E,V_b) = T_r(G^r \Gamma_L G^a \Gamma_R). \tag{3}$$

Here $G^{r(a)}$ is the retarded (advanced) Green's function of the midsection, and $\Gamma_{L(R)}$ is the contact broadening function of the left terminal (right terminal). It is known that the ideal thermoelectric material with maximum power-generation efficiency are given by[18]

$$\eta_{max} = \left(\frac{T_{hot}-T_{cold}}{T_{hot}}\right)\left[\frac{\sqrt{1+ZT}-1}{\sqrt{1+ZT}+(T_{cold}/T_{hot})}\right], \tag{4}$$

where T_{hot} and T_{cold} are the absolute temperatures of the left and right heat baths. Fixing T_{hot} and T_{cold}, the efficiency, η_{max}, is determined by the dimensionless figure of merit ZT,

$$ZT = TGS^2/(K_e + K_p), \tag{5}$$

where T is the temperature, G is the electronic conductance (which is the electronic current I generated for a given voltage V in a material and $G = I/V$), S is the Seebeck coefficient (which is the voltage V generated for a given temperature difference ΔT in a material and $S = V/\Delta T$), K_e is the electronic thermal conductance (which is the electron thermal current I_Q generated for a given temperature difference ΔT in a material and $K_e = I_Q/\Delta T$), and K_p is the lattice thermal conductance (which is the lattice thermal current J generated for a given temperature difference ΔT in a material and $K_p = J/\Delta T$). In the ballistic transport, an intermediate function[43] is introduced for expressing G, S, and K_e conveniently,

$$\Gamma^{(m)} = \frac{2}{h}\int_{-\infty}^{\infty}(E-\mu)^m\left[-\frac{\partial f(E,\mu,T)}{\partial E}\right]\tau_e(E)\mathrm{d}E. \tag{6}$$

Then the seebeck coefficient S, the conductance G, and the electron thermal conductance K_e can be expressed as

$$\frac{1}{eT}\frac{\Gamma^{(1)}}{\Gamma^{(0)}}, \quad e^2\Gamma^{(0)}, \quad \frac{1}{T}\left[\Gamma^{(2)} - \frac{\Gamma^{(1)}}{\Gamma^{(0)}}\right],$$

respectively. The phonon transmission function and phonon thermal conductance can be expressed as[44]

$$\tau(\omega) = \mathrm{Tr}(G^r \Gamma_L G^a \Gamma_R), \tag{7}$$

$$k_p = \frac{\hbar^2}{k_B T^2}\frac{1}{2\pi}\int_0^{\infty}\tau(\omega)\frac{\omega^2 \mathrm{e}^{\beta\hbar\omega}}{(\mathrm{e}^{\beta\hbar\omega}-1)^2}\mathrm{d}\omega. \tag{8}$$

Based on the above calculation, we can get ZT value. Some experimental efforts have been done by using graphene nanostructures for DNA sequencing, involving DNA passing through graphene nanopores, nanogaps, and nanoribbons. Most of the experimental and proposed work involving using recognition tunnelling to identify DNA nucleotides rely on hydrogen bonds, or other temporary interactions between the bases and electrodes. This is presumably for practical reasons: in order to sequence a strand of DNA it must be able to move through the tunnelling junction. Recently, He *et al.* succeeded in covalently linking porphines to graphene edges.[36] Xu *et al.* reported a robust approach to fabricate single-molecule transistors with covalent ZGNR–molecule–ZGNR chemical bonds, and current–voltage characteristics is measured steadily by experiment at room temperatures in ZGNR–molecule–ZGNR devices.[37] Merging these technologies, the behavior of electronic transport for different bases of DNA should be able to achieved experimentally. Some studies found that ZGNR have magnetic (or spin) states at their edges, and that these states can be either antiparallel or parallel.[45–47] Further studies showed that these states become unstable at room temperature.[46] So in our calculations, the spin polarization in the ZGNR-related systems is ignored. Since the experiment shows that the current–voltage characteristics have been measured as being stable at room temperature,[37] the optimized structures in our calculations should also reach a stable state at room temperature.[48–53]

3. Results and discussion

Figure 2 investigates the current values of *N*-ZGNR-*I*-(*j*) (*j* = a, b, or c) as a function of applied bias. Moreover, the current-voltage characteristics of the pristine 4-ZGNR, 5-ZGNR are also presented for comparison. It is interesting to find that different base devices exhibit different transport characteristics, although they have the same left and right electrodes. Clearly in Fig. 2(a), 4-ZGNR-*I*-(a) (*I* = A, G, and T) significantly improves the current value when the bias voltage is higher than certain threshold voltage, and the current value is even almost 3 times larger than the pristine 4-ZGNR at bias voltage 0.9 V in 4-ZGNR-A-(a). However, the current value of 4-ZGNR-C-(a) is far lower than that of the corresponding pristine 4-ZGNR. Moreover, another impressive characteristic is that the current values in 4-ZGNR-A-(a) and 4-ZGNR-A-(c) present obvious unsymmetry under opposite biases. Especially, the current values in 4-ZGNR-A-(c) are larger than those in pristine 4-ZGNR under negative biases while the current values in 4-ZGNR-A-(c) are much lower than those in pristine 4-ZGNR under positive biases. Relative to large differences of current–voltage characteristics in different base coupling systems with 4-ZGNR, the current values in 5-ZGNR-*I*-(*j*) are all much lower than those in pristine 5-ZGNR. These results indicate that the phenomenon of current–voltage characteristics in base-ZGNR coupling systems depends on the width of ZGNRs.

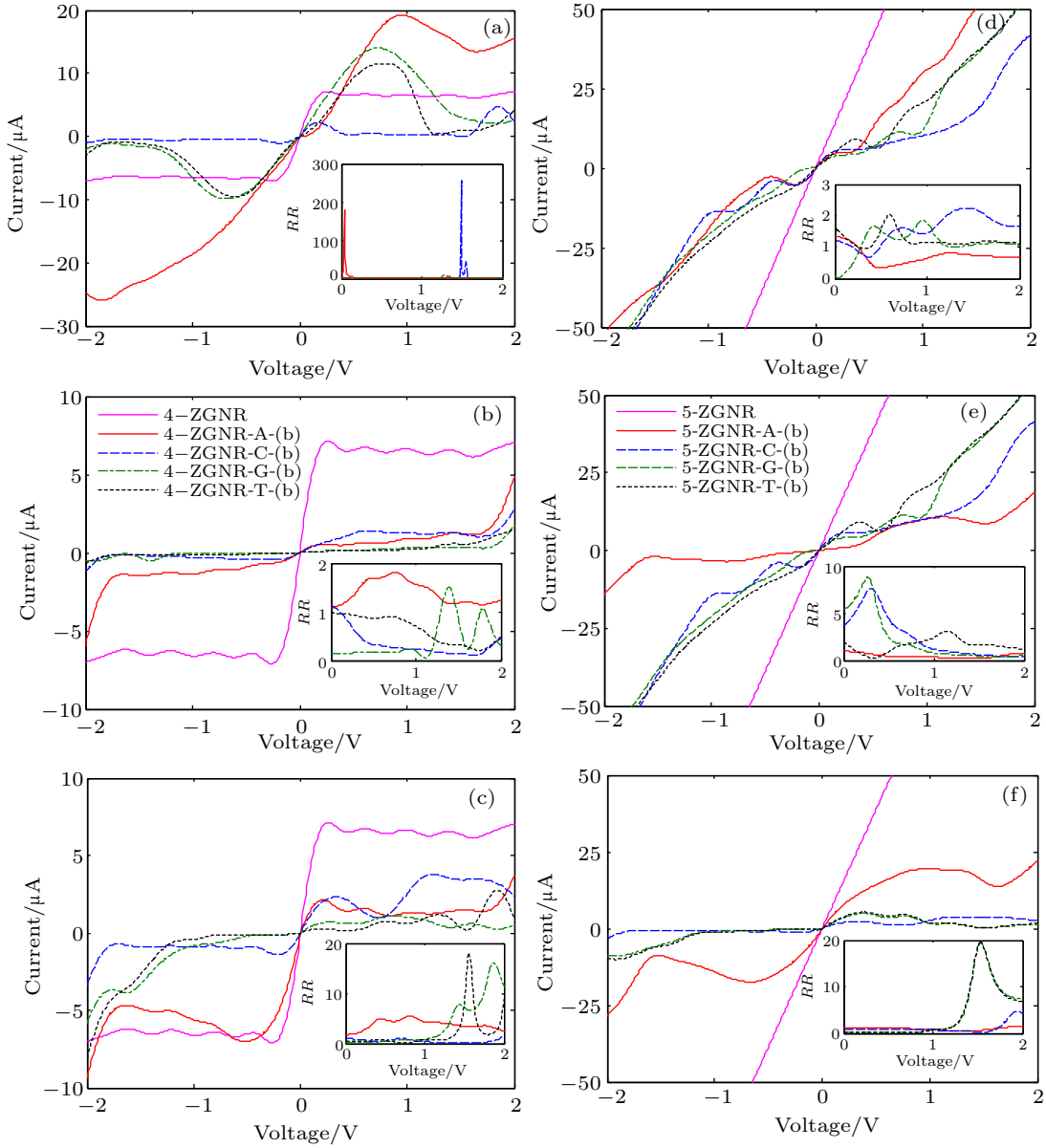

Fig. 2. Descriptions of the currents as a function of the applied bias of *N*-AGNR-*I*-(*j*). Purple solid, red solid, dashed, dotted, and dash-dotted curves in panels (a)–(f) correspond to the structures of pristine *N*-ZGNR, *N*-ZGNR-A-(*j*), *N*-ZGNR-C-(*j*), *N*-ZGNR-G-(*j*), and *N*-ZGNR-T-(*j*). Panels (a)–(c) correspond to 4-ZGNR-*I*-(a), 4-ZGNR-*I*-(b), and 4-ZGNR-*I*-(c); Panels (d)–(f) correspond to 5-ZGNR-*I*-(a), 5-ZGNR-*I*-(b), and 5-ZGNR-*I*-(c). The insets in panels (a)–(f) correspond to the rectification ratio *RR*.

Furthermore, another two interesting effects ca also be observed from these *I*–*V* curves: (i) Rectifying effect. The rectification ratio is defined as $RR = I(-V)/I(V)$, where $I(-V)$ and $I(V)$ correspond to the currents under negative and positive biases with the same voltage magnitude. From the inserts in Fig. 2, we can see clearly that the rectification effects in 4-ZGNR-A-(a) and 4-ZGNR-C-(a) are most obvious, and the largest rectification ratios reach 180 at 0.04 V in 4-ZGNR-A-(a) and 254 at 1.49 V in 4-ZGNR-C-(a). In addition, the rectifying behavior is also observed in other base devices. These behaviors mean that our base-ZGNR coupling systems can function as a good electronic rectifier. (ii) NDR effect. Clearly, NDR behavior can be observed in 4-ZGNR-*I*-(a) (I = A, G, and T) and 4-ZGNR-*I*-(c) (I = A and C). It is known that the NDR effect has very important application value in future electronic circuity, including fast switches, amplifiers, and memories.[23] For organic molecules, including microbial molecule, their molecular energy levels are discrete. In general, there is a large energy gap between the frontier molecular orbits, which results in a small total conductivity of the system. Furthermore, the degree of localization of molecular frontier orbitals also affects the conductivity of the system. So the current of molecular system is generally at the level of mA, or even lower. The rectifying property of the device is often due to the asymmetry of the system, or affected by the doping of the recipient and donor. In this work, the DNA bases contains *N* atom and other groups, which can be considered as acceptor doping. These bases have asymmetric structure, and the asymmetry of the base structure will also cause rectification effect. These base pairs are abundant in na-

ture. Their rectification effect can provide theoretical basis for their application in biological devices and electronic devices. Compare with H-bonding modalities between the nucleotides and the electrodes in similar systems, covalent bond in this paper is more permanent and the magnitudes of the observed currents in our systems are much greater. For example, the magnitude of the measured currents in hydrogen-bonded configuration lies in the range from a few nA to about a few pA. However, the magnitude of the currents in our systems lies in a few μA. The low currents are responsible for the weak interaction, which is also consistent with previous studies.[19] From the point of view of the difficulty of current detection, our model is easier to be detected. Especially, it is interesting to find that in Fig. 2(a), $I_{4-\mathrm{ZGNR-A-(a)}} > I_{4-\mathrm{ZGNR-C-(a)}} > I_{4-\mathrm{ZGNR-G-a)}} > I_{4-\mathrm{ZGNR-T-(a)}}$ within the applied-bias region [0.70 eV, 1.10 eV], which is consistent with the recognition tunneling currents by integrating over the 1-ps duration of the simulation in previous studies.[20] Recent researches found that thermoelectric conversion efficiency in different base-sandwiched systems displays different characteristics.[19] In theory, thermoelectric effects should also be able to sequence DNA. So, thermoelectric studies may provides novel opportunities for nanodevices for DNA sequencing. We look forward to progress in this area.

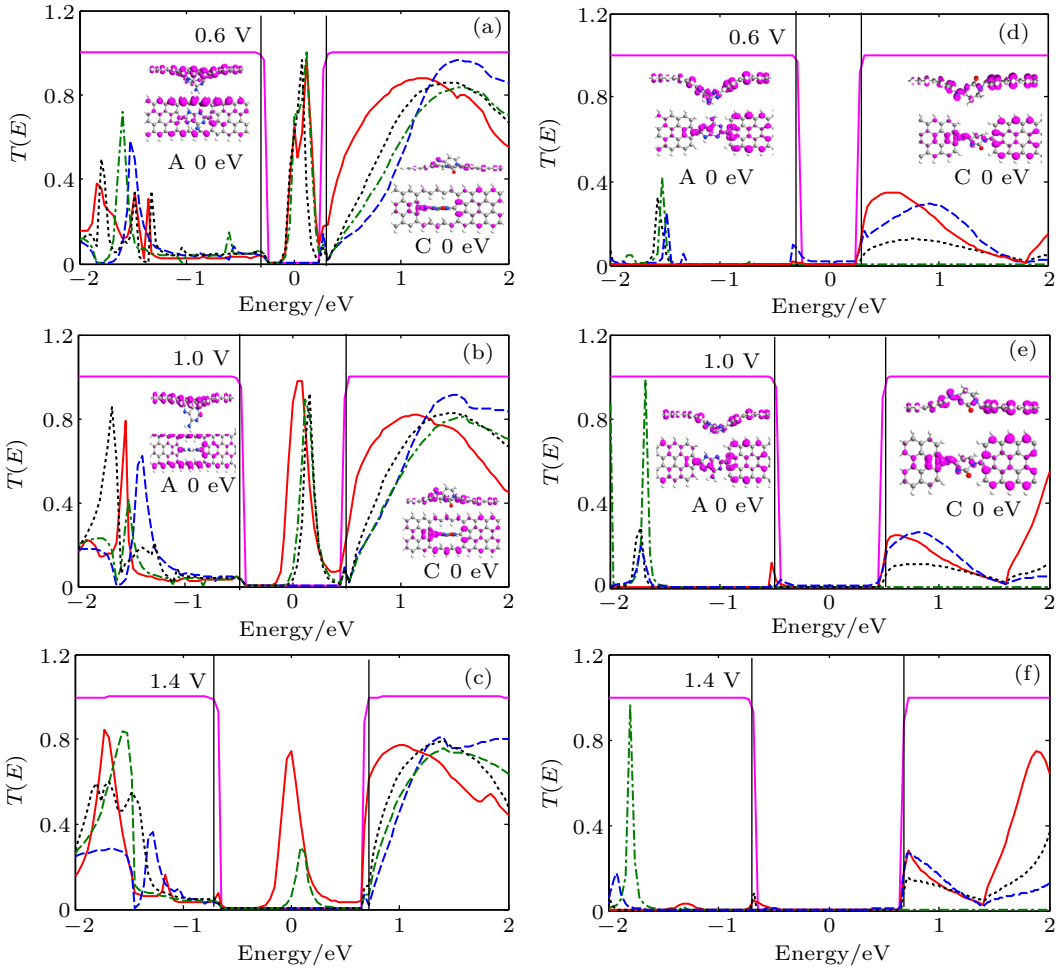

Fig. 3. Panels (a)–(c) [(d)–(f)] describe the electron transmission spectra of 4-ZGNR-*I*-(a) (4-ZGNR-*I*-(b)) at bias voltages 0.6 V, 1.0 V, and 1.4 V. Purple solid, red solid, dashed, dotted, and dash-dotted curves in panels (a)–(c) [(d)–(f)] correspond to the structures of pristine 4-ZGNR, 4-ZGNR-A-(a), 4-ZGNR-C-(a), 4-ZGNR-G-(a), and 4-ZGNR-T-(a) (4-ZGNR, 4-ZGNR-A-(b), 4-ZGNR-C-(b), 4-ZGNR-G-(b), and 4-ZGNR-T-(b)). The left and right insets of panels (a) and (b) [(d) and (e)] show the LDOSs of 4-ZGNR-A-(a) and 4-ZGNR-C-(a) (4-ZGNR-A-(b) and 4-ZGNR-C-(b)) at $E = 0$.

To understand the electron transport properties in different base devices, in Fig. 3, we calculate their transport spectra under different bias voltages. For brevity, only bias voltage 0.6 V, 1.0 V, and 1.4 V are considered here. For the symmetric pristine 4-ZGNR, a transmission gap is formed near the Fermi level due to π and π^* subbands have opposite σ parity and they cannot couple with each other to contribute to the transmission.[54] When the bases exist in scattering region (which breaks the electronic symmetry[54]), π and π^* subbands no longer have definite σ parity and can couple with each other, leading to big transmission coefficients near the Fermi level in 4-ZGNR-*I*-(a) (I = A, G, and T). However, the transmission coefficients in 4-ZGNR-C-(a) are very low near the Fermi level. In order to understand the divergence of the transmission coefficients, we display the local device density of states (LDOS) of 4-ZGNR-A-(a) and 4-ZGNR-C-

(a) in Fig. 3(a). LDOS analysis shows that the LDOS in 4-ZGNR-C-(a) is distributed unsymmetrically highly and also much weaker than that in 4-ZGNR-A-(a), which means the wave functions of the π subband from the left electrode hardly touch those of the π^* subband in the right electrode. So, the electrons from the left electrode scarcely cross the scattering region to the right electrode, and leading to a very low transmission coefficient in 4-ZGNR-C-(a). However, although the LDOS in 4-ZGNR-A-(a) is distributed unsymmetrically, the distribution of LDOS along the edges is very symmetric, and the wave functions of the π subband from the left electrode can couple with those in the right electrode by the edge states, forming a perfect transport channel in the edge and resulting in a big transmission coefficient. Increasing the bias voltage from 0.6 V to 1.0 V, a wider peak of 4-ZGNR-A-(a) and narrower peaks of 4-ZGNR-G-(a) and 4-ZGNR-T-(a) appear in the bias window. Therefore, the current of 4-ZGNR-A-(a) is further increased, while the currents of 4-ZGNR-G-(a) and 4-ZGNR-T-(a) are decreased, which induces the NDR behavior in 4-ZGNR-G-(a) and 4-ZGNR-T-(a). Further increasing the bias voltage from 1.0 V to 1.4 V, the transmission coefficients of these base systems are all suppressed obviously. So the currents are also decreased and the NDR behavior occurs in 4-ZGNR-A-(a). Compared the transport spectra of 4-ZGNR-*I*-(b)s with those of 4-ZGNR-*I*-(a)s at the same bias voltage, the main divergence is that the transmission coefficients of 4-AGNR-*I*-(b)s in the bias window are very low.

In order to understand the low transmission coefficients of 4-AGNR-*I*-(b)s, the LDOSs of 4-ZGNR-A-(b) and 4-ZGNR-C-(b) are presented in the insets of panels (d) and (e). Clearly, the LDOSs in 4-ZGNR-C-(b) and 4-ZGNR-A-(b) are distributed unsymmetrically highly compared with that in 4-ZGNR-A-(a), the weak wave functions overlap hinders carrier injection from the left electrode to the base and finally to the right electrode. This phenomenon indicates very low transmission coefficients in 4-ZGNR-*I*-(b)s. Increasing the bias, enlarging the range of transport spectra in the bias window, and forming greater current values in all 4-ZGNR-*I*-(b)s. Another interesting discovery is the significantly rectifying characteristic, which further broadens electronic applications of base-ZGNR coupling devices in a new generation of electronic circuity. In the present work, although large rectifying effect occurs at some biases in Figs. 2(a) and 2(d), the current values at these biases are $\rightarrow 0$. So, the applications of theses devices are restricted. Especially, in strong contrast to low current values in 4-ZGNR-*I*-(c) (I = C, G, and T), the current in 4-ZGNR-A-(c) is comparable with that in pristine 4-ZGNR and a big rectifying effect can also be observed in this structure (the $RR = 4.92$ at 0.45 eV, and $RR = 5.4$ at 0.82 eV). To understand these interesting effects, we describe electron transmission spectra for 4-ZGNR-A-(c) at 0.2 V, 0.4 V, and 0.8 V biases in Figs. 4(a)–4(c). As a comparison, in Figs. 4(e)–4(g), we describe electron transmission spectra for the same structure at opposite biases. Clearly from Figs. 4(a) and 4(d), the transmission coefficients in 4-ZGNR-A-(c) at 0.2 V are much lower than those in 4-ZGNR-A-(c) at -0.2 V within bias window, which induces much lower current at 0.2 V than -0.2 V. When the bias is changed from -0.2 V to -0.4 V, the region with big transmission coefficients are also widened in the increased bias window. So, the current value increases from 4.96 μA to 6.77 μA. However, when the bias is increased from 0.2 V to 0.4 V, the transmission coefficients near the right chemical potential decrease obviously. Though the low transmission region also widens as the bias voltage increases, the increased low transmission region cannot compensate for the loss. Therefore, the current value decreases from 2.11 μA to 1.44 μA, leading to the appearance of NDR at positive biases and large rectifying ratio. When the bias is changed from 0.4 V to 0.8 V and -0.4 V to -0.8 V, although the increased bias window both contains lesser transmission coefficients, the strength of the scattering in the structure with positive bias is much stronger than that with negative bias, giving larger rectifying ratio. The rectifying effect can be understood with the help of the schematic LDOSs in these structures. Clearly from the insets in Fig. 4, the distribution of LDOSs at negative bias is more symmetric than that at positive bias in the same structures, which means that the carrier can more easily pass through the base-ZGNR coupling systems at negative bias, and forming obvious rectifying effect. Clearly, comparing the rectification ratio *RR* in 4-ZGNR-A-(c), the most striking difference is that the rectification peak of RR in 4-ZGNR-T-(c) and 4-ZGNR-G-(c) occurs at big bias [see Fig. 2(c)]. The transport spectra under different negative bias shown in Fig. 4 illustrate this interesting phenomenon. Obviously in Figs. 4(e)–4(g), the transmission peak only exists at low energy with negative bias in 4-ZGNR-A-(c). So, the rectification peak just exists at low bias. However, the transmission peak only exists at large energy of electron with negative bias in 4-ZGNR-T-(c) and 4-ZGNR-G-(c) [see Figs. 4(d) and 4(h)], which results in that big *RR* only happens at large bias.

It is known that the covalent bond is generally more permanent in nature than the H-bond. Some studies focused on single-molecule devices rely on covalent bond coupling. While many studies involving using recognition tunnelling to identify DNA nucleotides rely on hydrogen bonds. It would be very interesting and important to do a comparison analysis contrasting their electrical transport properties. So, as a comparison with the current in 4-ZGNR-*I*-(b) (I = A, C, G, and T)), we study I–V curves of 4-ZGNR-A-(h), 4-ZGNR-C-(h), 4-ZGNR-G-(h), and 4-ZGNR-T-(h). (note that the bond between the bases and electrodes is H-bond in 4-ZGNR-*I*-(h)

(I = A, C, G, and T)). It is found from Fig. 5(a) that the current values in 4-ZGNR-I-(h) are less than 0.5 nA even the voltage reaches 2 V, which are similar to previous DNA sequencing studies[55–59] and much smaller than those in 4-ZGNR-I-(b). The reason can be revealed from the LDOS at the insets in Fig. 5(a). Clearly, due to the absence of electronic states in many atom positions of 4-ZGNR-I-(h), the wave functions of the electron states from the left electrode cannot touch those of the wave functions of the electron states in the right electrode. So, the electron from the left electrode can hardly cross the scattering region to the right electrode. As a result, the current is very low in H-bond coupling structures.

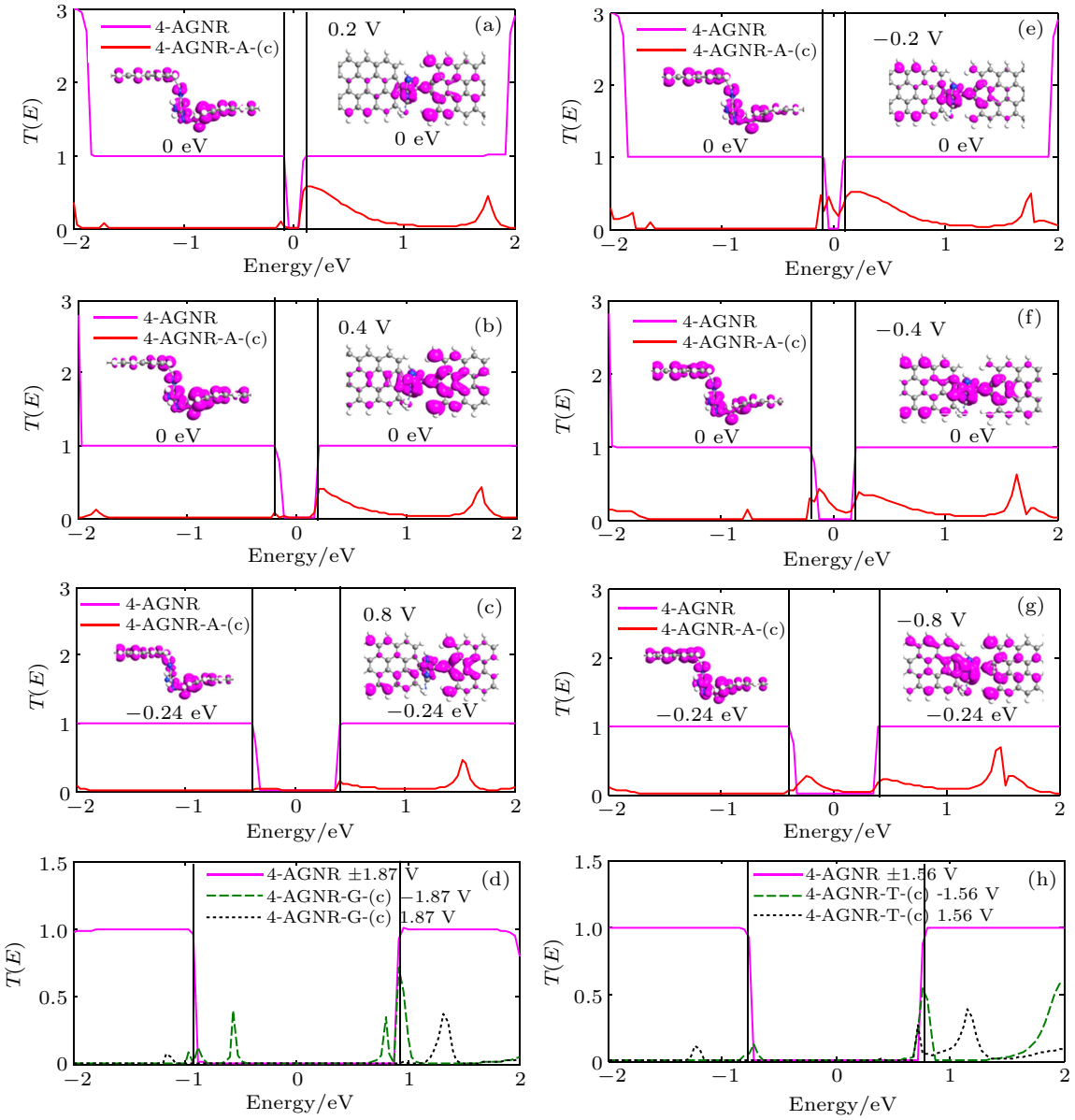

Fig. 4. Panels (a)–(c) [(e)–(g)] describe the electron transmission spectra at bias voltages 0.2 V, 0.4 V, and 0.8 V (at bias −0.2 V, −0.4 V, and −0.8 V). Purple solid and red solid curves in panels (a)–(c) and (e)–(g) correspond to the structures of pristine 4-ZGNR and 4-ZGNR-A-(c). The insets of panels (a)–(b) and (e)–(f) show the LDOSs of 4-ZGNR-A-(c) at $E = 0$, and The insets of panels (c) and (g) show the LDOSs of 4-ZGNR-A-(c) at $E = -0.24$ eV. Solid, dashed, and dotted curves in panel (d) [(h)] describe the electron transmission spectra in pristine 4-ZGNR at bias 1.87 V, 4-ZGNR-G-(c) at bias 1.87 V, and 4-ZGNR-G-(c) at bias −1.87 V (pristine 4-ZGNR at bias 1.56 V, 4-ZGNR-T-(c) at bias 1.56 V, and 4-ZGNR-T-(c) at bias −1.56 V).

Meanwhile, it is also noted that although the current is low and there is no negative differential effect, the current $I_{4-\mathrm{ZGNR}-\mathrm{T}-(\mathrm{h})} > I_{4-\mathrm{ZGNR}-\mathrm{C}-(\mathrm{h})} > I_{4-\mathrm{ZGNR}-\mathrm{A}-(\mathrm{h})} > I_{4-\mathrm{ZGNR}-\mathrm{G}-(\mathrm{h})}$, which means that the base can be easily distinguished by the current value. Then, we analyze the I–V curves of 4-ZGNR-I-(f) (I = A, C, G, and T)). In these structures, the bases are designed to couple with deoxynucleotides and then covalently bonded with left and right N-ZGNR electrodes. Figure 5(b) shows that the current $I_{4-\mathrm{ZGNR}-I-(\mathrm{f})} > I_{4-\mathrm{ZGNR}-I-(\mathrm{h})}$. Larger currents may be responsible for the stronger interaction, namely the covalent bonds between the left and right N-ZGNR electrodes. To confirm this hypothesis, the LDOS of 4-ZGNR-I-(f) are plotted in the insets of Fig. 5(b). It is Clearly seen from the inserts in Fig. 5(b) that, due to the existence of electronic states in more atom positions of 4-ZGNR-I-(f), this well-proportioned distribution of

LDOS is advantageous for electron going through the system more smoothly. As a result, the current in 4-ZGNR-*I*-(f) is larger than that in 4-ZGNR-*I*-(h). In addition, although the bonds between the scattering region and the left (right) electrodes are covalent in 4-ZGNR-*I*-(b) and 4-ZGNR-*I*-(f), due to more atoms in the scattering region in 4-ZGNR-*I*-(f), the electrons are more easily scattered by the scattering region, which induces the current $I_{4-\mathrm{ZGNR}-i-(\mathrm{b})} > I_{4-\mathrm{ZGNR}-i-(\mathrm{f})}$.

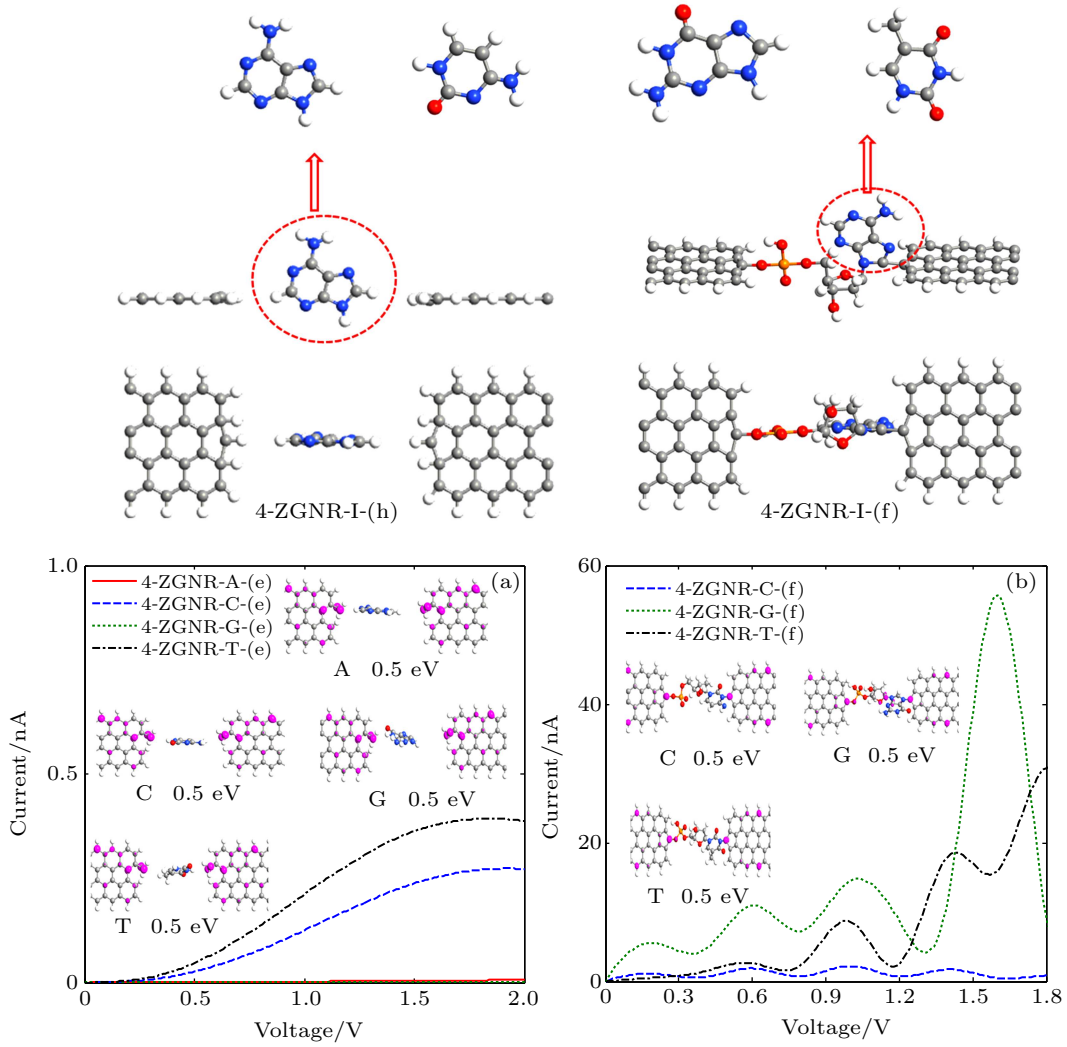

Fig. 5. Description of the currents as a function of the applied bias of 4-ZGNR-*I*-(h) and 4-ZGNR-*I*-(f) in panels (a) and (b). Purple solid, dashed, dotted, and dash-dotted curves in panel (a) correspond to the structures of *N*-ZGNR-A-(h), *N*-ZGNR-C-(h), *N*-ZGNR-G-(h), and *N*-ZGNR-T-(h). Purple solid, dashed, dotted, and dash-dotted curves in panel (b) correspond to the structures of *N*-ZGNR-A-(f), *N*-ZGNR-C-(f), *N*-ZGNR-G-(f), and *N*-ZGNR-T-(f). The insets in panels (a)–(b) correspond to the LDOS at $E = 0.5$ eV.

Clearly from Figs. 2(a) and 2(c), another impressive characteristic is the currents enhancement in 4-ZGNR-A-(a) and 4-ZGNR-A-(c), and the currents are even much bigger than those in pristine 4-ZGNR at some biases. So, we judge that the coupling between the base A and ZGNR should be excellent thermoelectric performance. Recently, the current–voltage characteristics is measured steadily by experiment at room temperatures in ZGNR–molecule–ZGNR devices. The room temperature is experimentally feasible to study thermoelectric performance in base-ZGNR coupling devices. So in the following study, we focus on the thermoelectric performance in this coupling system in Fig. 6 at room temperatures. It can be found that in perfect 4-ZGNR, the phonon transmission coefficient is of quantum character, and the phonons can be transported perfectly without scattering. While the phonon transmission coefficients of 4-ZGNR-A-(d) and *N*-ZGNR-A-(e) ($N = 4$ and 5) exhibit many peak-dip structures, and are much lower than those of the pristine 4-ZGNR due to the structure scattering. So, the thermal conductances in these structures are decreased obviously. In order to measure the reduction degree in the thermal conductance of *N*-ZGNR-A-i, the ratio, $\zeta_i = k_i/k_{\mathrm{N-ZGNR}}$ (i is *N*-ZGNR-A-(d) or *N*-ZGNR-A-(e) ($N = 4$ and 5)), is defined. Clearly from the inset of Fig. 6(b), the ratio is lower than 0.1 in the temperature $0 \leftrightarrow 500$ K in 4-AGNR-A-(d), and even lower 0.05 in *N*-ZGNR-A-(e) ($N = 4$ and 5). The very low thermal condctances can bring a strong advantage to high ZT discussed later. In addition, ZT also depends strongly on the seebeck coefficient S. It can be found

from the inset of Fig. 6(c) that the electron transmission function for perfect 4-ZGNR shows some smooth stepwise platforms, which implies that electrons can pass through the pristine 4-ZGNR without any scattering. However, when the base A exists in scattering region, Similar to phonon transport, the stepwise platforms are dramatically destroyed, and the electron transmission coefficients show some peak-dip structures. Especially, theses electronic transmission mutates induce the high peak of seebeck coefficient S, which is also fully consistent with the Cutler–Mott formula[1–3]

$$(T,\psi) \approx \frac{\pi^2 k_{\mathrm{B}}^2}{3e} \frac{\partial \ln T_{\mathrm{e}}}{\partial E}. \tag{9}$$

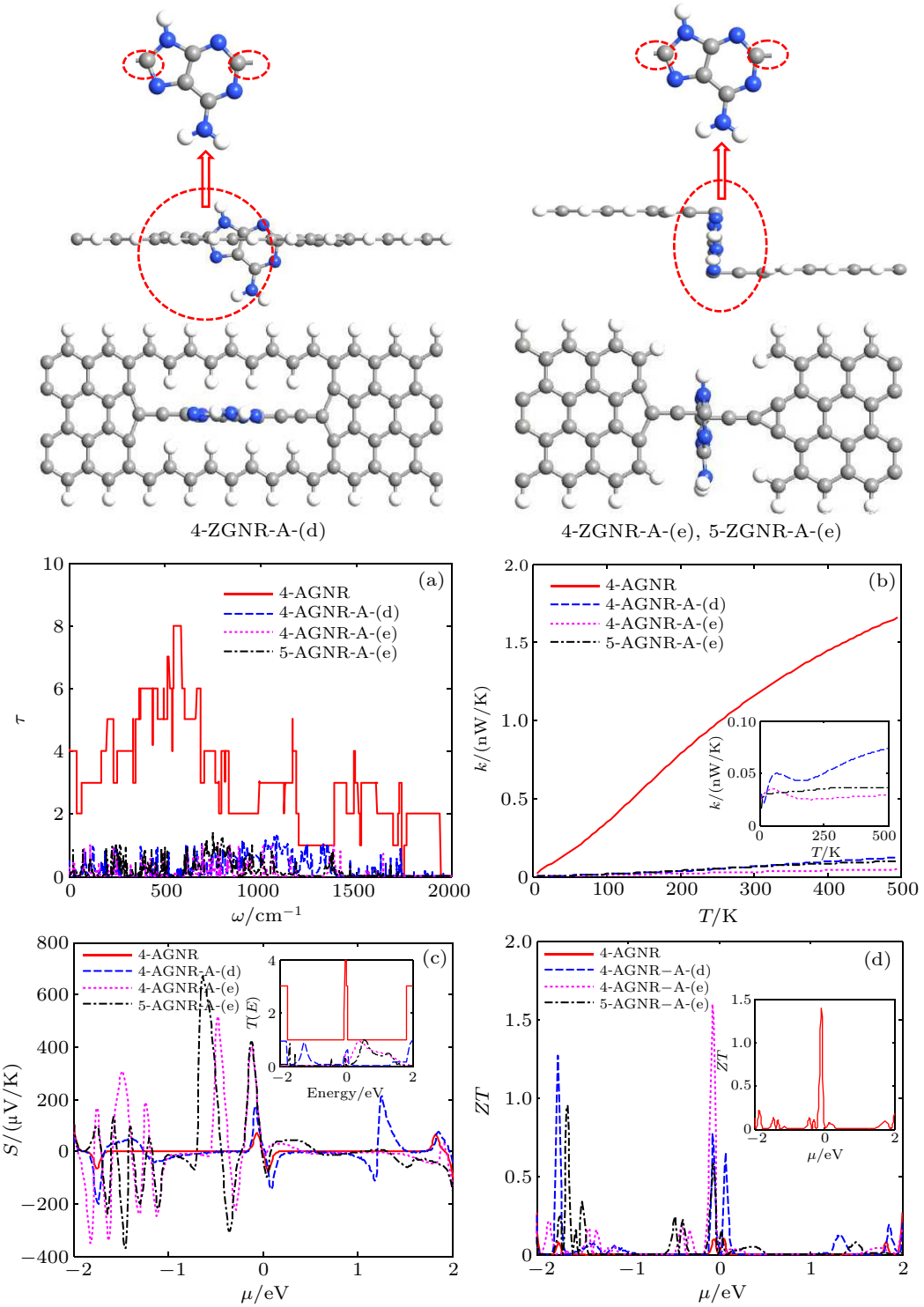

Fig. 6. Panels (a), (b), (c), and (d) describe the phonon transmission, thermal conductance, Seebeck coefficient, and ZT values of N-ZGNR-A-(i) (i = d and e) at temperature 200 K, respectively. Solid, dashed, dotted, and dash-dotted curves in panels (a), (b), (c), and (d) correspond to 4-ZGNR, 4-ZGNR-A-(d), 4-ZGNR-A-(e), and 5-ZGNR-A-(e). The inset in panel (b) corresponds to the thermal conductance ratio $\eta(T) = k_i/k_0$, and the dashed, dotted, and dash-dotted curves correspond to 4-ZGNR-A-(d), 4-ZGNR-A-(e), and 5-ZGNR-A-(e). The inset in panel (c) corresponds to the electron transmission spectra, and the solid, dashed, dotted, and dash-dotted curves correspond to 4-ZGNR, 4-ZGNR-A-(d), 4-ZGNR-A-(e), and 5-ZGNR-A-(e). The inset in panel (d) corresponds to the ZT value of 4-ZGNR-A-(e) at temperature 300 K.

Although the base A can induce low phonon thermal conductance k_{ph}, electric thermal conductance k_e, electric conductance σ, and also high peak S, the $S^2\sigma T/(k_{ph}+k_e)$ will win the competition with σ. As a consequence, the $ZT = S^2\sigma T/(k_{ph}+k_e)$ will reache a much bigger value in N-ZGNR-A-(i) than that in pristine N-ZGNR, and the ZT_{max} hits 1.6 at temperature 200 K in 4-ZGNR-A-(e), which is much bigger than the maximum value (= 0.09) of ZT in perfect 4-ZGNR pristine.[60]

4. Conclusion and perspectives

In summary, we investigated the electronic, thermal, and thermoelectric properties in the A, G, C, and T bases perpendicularly coupling between two N-ZGNR electrodes by using nonequilibrium Green's functions in combination with the density-functional theory. The results show that the currents in different base-ZGNR coupling systems display different current bias voltage characteristics, and the base-ZGNR coupling system can present large RE and NDR effects. These interesting results are well explained in terms of the transmission spectrum and the spatial distribution of LDOS. Moreover, due to the fluctuations of electron transmission and the reduction of the phonon thermal conductance, the ZT is improved significantly: the ZT_{max} will be over 1.4 at room temperature, and over 1.6 at 200 K. Our results will be helpful for designing and fabrication of high-performance switches, memories, and thermoelectric devices.

References

[1] Tao N J 2006 *Nat. Nanotechnol.* **1** 173
[2] Angione M D, Pilolli R, Cotrone S, *et al.* 2011 *Mater. Today.* **14** 424
[3] Aradhya S V and Venkataraman L 2013 *Nat. Nanotechnol.* **8** 399
[4] Yee S K, Sun J, Darancet P, Tilley T D, Majumdar A and Neaton J B 2011 *ACS Nano* **5** 9256
[5] Capozzi B, Xia J, Adak O, *et al.* 2015 *Nat. Nanotechnol.* **10** 522
[6] Cao H, Ma J and Luo Y 2010 *Nano Res.* **3** 350
[7] Chen L, Hu Z, Zhao A, Wang B, Luo Y and Yang J 2007 *Phys. Rev. Lett.* **99** 146803
[8] Geng H, Hu Y, Shuai Z, Xia K, Gao H and Chen K 2007 *J. Phys. Chem. C* **111** 19098
[9] Fan Z Q, Zhang Z H, Deng X Q, Tang G P, Yang C H, Sun L and Zhu H L 2016 *Carbon* **98** 179
[10] Kuang G, Chen S Z, Wang W, Lin T, Chen K, Shang X, Liu P N and Lin N 2016 *J. Am. Chem. Soc.* **138** 11140
[11] Wu D, Cao X H, Chen S Z, Tang L M, Feng Y X, Chen K Q and Zhou W X 2019 *J. Mater. Chem. A.* **7** 19037
[12] Liu Y Y, Zeng Y J, Jia P Z, *et al.* 2018 *J. Phys.: Condens. Matter* **30** 275701
[13] Li Q, Tang L, Zhang C, *et al.* 2017 *Appl. Phys. Lett.* **111** 171602
[14] Wu D, Cao X H, Jia P Z, *et al.* 2020 *Sci. China-Phys. Mech. Astron.* **63** 276811
[15] Zeng Y J, Wu D, Cao X H, *et al.* 2020 *J. Mater. Chem. A* **8** 11884
[16] Liang L and Meunier V 2013 *Appl. Phys. Lett.* **102** 143101
[17] Xu Y, Li Z and Duan W 2014 *Small* **10** 2182
[18] He J and Tritt T M 2017 *Science* **357** 1369
[19] Gao R B, Peng X F, Jiang X T, Tan X H and Long M Q 2019 *Org. Electron.* **67** 57
[20] Krstić P, Ashcroft B and Lindsay S 2015 *Nanotechnology* **26** 084001
[21] Russ B, Glaudell A, Urban J J, Chabinyc M L and Segalman R A 2016 *Nat. Rev. Mater.* **1** 16050
[22] Zhang Q, Sun Y, Xu W and Zhu D 2014 *Adv. Mater.* **26** 6829
[23] Wu Q H, Zhao P, Liu D S, Li S J and Chen G 2014 *Org. Electron.* **15** 3615
[24] Chen J, Walther J H and Koumoutsakos P 2014 *Nano Lett.* **14** 819
[25] Liu X, Zhang G and Zhang Y W 2016 *Nano Lett.* **16** 4954
[26] Peng X F, Chen KQ, Wang XJ and Tan S H 2016 *Carbon* **100** 36
[27] Lv R, Chen G, Li Q and McCreary A, *et al.* 2015 *Proc. Natl. Acad. Sci. USA* **112** 14527
[28] Xu Y F, Liu Z B, Zhang X L, Wang Y, Tian J G, Huang Y, Ma Y F, Zhang X Y and Y S 2009 *Adv. Mater.* **21** 1275
[29] Zeng J, Chen K Q and Tong Y X 2018 *Carbon* **127** 611
[30] Xiao N, Dong X, Song L, Liu D, *et al* 2011 *ACS Nano* **5** 2749
[31] Hang P H, Bahramy M S, Nagaosa N and Nikolić B K 2014 *Nano Lett.* **14** 3779
[32] Tan S H and Chen K Q 2015 *Carbon* **94** 942
[33] Heerema S J and Dekker C 2016 *Nat. Nanotechnol.* **11** 127
[34] Zeng J, Chen K Q, He J, Fan Z Q and Zhang X J 2011 *J. Appl. Phys.* **109** 124502
[35] Zeng J, Chen K Q, He J, Zhang X J and Sun C Q 2011 *J. Phys. Chem. C* **115** 25072
[36] He Y, Garnica M, Bischoff F, Ducke J, Bocquet M L, Batzill M, Auwärter W and Barth J V 2017 *Nat. Chem.* **9** 33
[37] Xu Q, Scuri G, Mathewson C, Kim P, Nuckolls C and Bouilly D 2017 *Nano Lett.* **17** 5335
[38] Baghsiyahi F B, Akhtar A and Yeganeh M 2018 *Int. J. Mod. Phys. B* **32** 1850207
[39] Büttiker M, Imry Y, Landauer R and Pinhas S 1985 *Phys. Rev. B* **31** 6207
[40] Taylor J, Guo H and Wang J 2001 *Phys. Rev. B* **63** 121104
[41] Taylor J, Guo H and Wang J 2001 *Phys. Rev. B* **63** 245407
[42] Brandbyge M, Mozos J L, Ordejón P, Taylor J and Stokbro K 2002 *Phys. Rev. B* **65** 165401
[43] Jiang J W, Wang J S and Li B 2011 *J. Appl. Phys.* **109** 014326
[44] Wang J S, Wang J and Lü J T 2008 *Eur. Phys. J. B* **62** 381
[45] Shen L, Zeng M, Li S, Sullivan M B and Feng Y P 2012 *Phys. Rev. B* **86** 115419
[46] Kim W Y and Kim K S 2008 *Nat. Nanotech.* **3** 408
[47] Son Y W, Cohen M L and Louie S G 2006 *Nature* **444** 347
[48] Zhang P P, Tan S H, Long M Q and Peng X F 2019 *Appl. Phys. Express* **12** 125005
[49] Wang Z Q, Tang F, Dong M M, *et al.* 2020 *Chin. Phys. B* **29** 067202
[50] Fan Z Q, Zhang Z H, Xie F, *et al.* 2015 *Org. Electron.* **18** 101
[51] Chen X K and Chen K Q 2020 *J. Phys.: Condens. Matter* **32** 153002
[52] Zhang G P, Mu Y Q, Zhao J M, *et al.* 2019 *Physica E* **109** 1
[53] Mu Y Q, Zhao J M, Chen L Y, *et al.* 2020 *Org. Electron.* **81** 105665
[54] Li Z, Qian H, Wu J, Gu B L and Duan W H 2008 *Phys. Rev. Lett.* **100** 206802
[55] Im J, Sen S, Lindsay S and Zhang P 2018 *ACS Nano* **12** 7067
[56] Shendure J, Balasubramanian S, Church G M, *et al.* 2017 *Nature* **550** 345
[57] Chang S, Shuo H S, He J, Liang F, Zhang P and Li S 2010 *Nano Lett.* **10** 1070
[58] Huang S, He J, Chang S, Zhang P, Liang F, Li S, Chen X, Sankey O and Lindsay S 2010 *Nano Lett.* **5** 868
[59] Tsutsui M, Taniguchi M, Yokota K and Kawai T 2010 *Nat. Nanotechnol.* **5** 286
[60] Pan C N, Xie Z X, Tang L M and Chen K Q 2012 *Appl. Phys. Lett.* **101** 103115